



ELSEVIER

Contents lists available at ScienceDirect

Surface & Coatings Technology

journal homepage: www.elsevier.com/locate/surfcoat

Process parameter optimisation of laser clad iron based alloy: Predictive models of deposition efficiency, porosity and dilution

L. Reddy^a, S.P. Preston^b, P.H. Shipway^a, C. Davis^c, T. Hussain^{a,*}^a Faculty of Engineering, The University of Nottingham, University Park, Nottingham NG7 2RD, UK^b School of Mathematics, The University of Nottingham, University Park, Nottingham NG7 2RD, UK^c Materials and Corrosion Team, Uniper Technologies Limited, Technology Centre, Ratcliffe on Soar, Nottingham NG11 0EE, UK

ARTICLE INFO

Keywords:

Process modelling
 NanoSteel
 Laser cladding
 Porosity
 Dilution
 Boiler coatings

ABSTRACT

As a candidate coating material for heat-exchanger surfaces in commercial power generation boiler, an amorphous/glass forming Fe-Cr-B alloy NanoSteel SHS 7170 was deposited by a 2 kW fibre laser onto a boiler grade steel substrate (15Mo3). A comprehensive trial with 28 single track optimisation runs was carried out to develop models of the influence of three processing parameters, laser power, laser traverse speed and powder feed rate, on powder deposition efficiency, dilution and porosity. It was found that deposition efficiency is dependent on laser power and powder feed rate, increasing with increasing power and decreasing powder feed rate when tested within the parameter window of laser power ranging from 0.4 to 2 kW; traverse speed varying from 150 to 1200 mm min⁻¹; and powder feed rate varying from 4 to 10 g min⁻¹. Similarly, it was found that dilution is also dependent on laser power and powder feed rate. Dilution increases with increasing power and decreases with increasing powder feed rate within the same parameter window discussed above. This means that through processing parameter selection, these properties can be adjusted to suit their application. Porosity was found to be independent of processing parameters and instead mostly dependent on the feedstock material. A model was produced for predicting porosity within a powder feedstock, found to be 8.5%. These models were used to successfully produce an optimised coating.

1. Introduction

The use of advanced coatings in industrial applications is both critical and widespread. Coatings find many uses in industries varying from conventional power generation, renewable energy, oil and gas, automotive, aerospace, mining, iron and steel to outer space. Coatings can offer a low cost alternative to bulk material components, or can allow the advantages of two different materials with unique properties to be combined into a single unit. Candidate coating materials are often highly alloyed or contain exotic elements to provide specialised performance. Laser cladding is a weld type coating deposition technique in which a high energy laser is passed over the surface of a substrate, creating a melt pool. The cladding material, in the form of either powder or wire, if fed into this melt pool, forms a metallurgical bond once solidified.

As a technique that has wide spread usage, there is obviously interest in producing predictive models for the coating characteristics of laser cladding. There are three main properties that need to be considered when producing coatings; the clad dimensions, dilution and porosity. Dilution is the mixing of the substrate material with the

coating material altering composition which could ultimately be deleterious to performance. Attempts to model these properties, and others such as feed geometries and stand-off distances have been carried out previously [1,2]. A popular technique used is linear regression through a trial and error approach. Whilst these techniques can agree on which parameters have an influence on coating deposition, they differ vastly in the influence these parameters play. Whilst these models may explain empirical results, [3] showed that the models vary vastly between coating and substrate materials, and even vary within the same materials. The influence of traverse speed on clad height for example can range from v^{-1} to $v^{-5/4}$ [4–6]. Other statistical empirical techniques have also been employed [7,8]. Analysis of variance (ANOVA) was used to model the deposition of a titanium alloy onto a substrate of the same composition [7]. The importance each variable plays in these models vary vastly from the models mentioned above. As well as these statistical models, theoretical models exist; these are primarily focused on laser processing technologies in a broader context, but obviously have applications for laser cladding [8].

The capture efficiency is simple to calculate empirically, however attempts to model the capture efficiency can be made through

* Corresponding author.

E-mail address: tanvir.hussain@nottingham.ac.uk (T. Hussain).<https://doi.org/10.1016/j.surfcoat.2018.05.054>

Received 22 December 2017; Received in revised form 1 May 2018; Accepted 26 May 2018

Available online 26 May 2018

0257-8972/ © 2018 The Authors. Published by Elsevier B.V. This is an open access article under the CC BY license (<http://creativecommons.org/licenses/by/4.0/>).

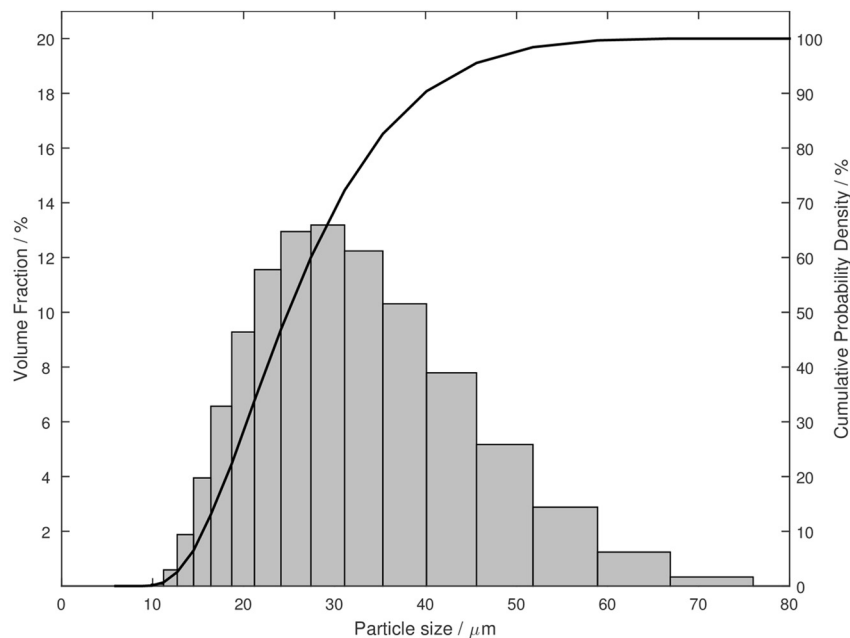


Fig. 1. Particle size distribution of NanoSteel SHS 7170 powder showing both volume fraction and cumulative volume fraction. The powder has a D50 of 28.2 μm , D90 of 45.3 μm and D10 of 17.6 μm .

consideration of energy balance. Previous work looking at the energy balance in laser processing has focused on its application in calculating melt depth and profile. Others have found application for the technique specifically in laser cladding and for calculating clad geometry in multi pass setups [9]. Another approach to predict capture efficiency is to look at powder feed geometry. Models have shown that beam divergence and variations in particle size will attenuate the beam by differing amounts [10]. This differing energy can be taken into account when looking at energy balance models. As capture efficiency is a problem that will only affect powder fed laser cladding systems, not wire fed setups.

A breadth of dilution models draw on original mathematical work on laser hardening [11]. This work models heat flow within a substrate under Gaussian and non-Gaussian sources, and was later built on using classical heat flow equations in two dimensions using a rectangular source [12]. Whilst looking only at laser surface treatment and not specifically laser cladding, the numerical calculations were able to predict melt depth and heat affected zones. These numerical models have been built upon to further improve their applicability, such as by modifying the geometry of the laser source beam to more closely match different experimental setups, and moving the models from the numerical, to analytical regimes [8]. Others, using the same fundamental work with the classical heat flow equations have produced semi-empirical models to predict the melt profile of multi-pass laser processing techniques.

Mathematical porosity modelling looked at two types of porosity; inter-run porosity and porosity within the feedstock powder. Inter-run porosity occurs when a gap is formed between successive depositions in multi clad coatings. This problem occurs predominantly in wire fed systems. It has been shown that this type of porosity can be minimised by keeping the clad bead contact angle below a critical level, dependent on the other coating parameters [4]. The technique used in this work for calculating porosity involves estimating powder pore size. The problem of estimating true volume distributions from cross sectional images of discrete particles is well established. The basis of estimating volume of regular particles [13] was used to develop key models in estimating the weighted volume by mean bisector of randomly shaped particles [14]. These methods were used for biological measurement; however has found application across a range of fields, including recently in grain size measurements.

In this work, single track trials of NanoSteel SHS 7170 were applied using a 2 kW fibre laser onto a carbon steel substrate. These were analysed using optical and scanning electron microscopy so that theoretical-empirical models of the influence of key coating parameters (deposition efficiency, dilution and porosity) on the final clad can be produced. The aim of this work was to develop a mathematical model to optimise NanoSteel SHS 7170 coating that can also be translated to other materials without significant modification. The ultimate goal was to develop optimised overlap coatings with desired characteristics and performance.

2. Experimental method

2.1. Materials

The Fe-based alloy powder SHS 7170 (The NanoSteel Company Inc., RI, USA) was used as a feedstock. The composition was measured by X-ray Fluorescence (XRF), Inductively Coupled Plasma Mass Spectroscopy (ICP-MS), and combustion methods to be Cr 20.3, W 6.3, B 3.6, Mn 2.1, Mo 4.8, C 1.0, Si 1.6 and Fe Bal. (all in wt%) [15]. A 15Mo3 substrate was used which has the nominal composition Fe 98.3, Cr 0.2, W 0.1, Ni 0.1, Mn 0.4, Mo 0.3, C 0.2, Si 0.2 and Cu 0.2 (all in wt%) [16].

2.2. Powder size characterisation

The size distribution of the powder was measured using laser diffractometry in a Mastersizer 3000 (Malvern Instruments, UK). The powder had a supplier provided size fraction of +15–53 μm . The Mastersizer measurement shows the feedstock had an average particle size of 28.2 μm and 10% of particles were smaller than 17.6 μm and 90% smaller than 45.3 μm . This distribution is shown in Fig. 1.

2.3. Laser cladding of coating

The powder was deposited onto a 200 mm \times 30 mm \times 6 mm 15Mo3 substrate using a 2KW Ytterbium doped fibre laser (IPG Photonics, Germany) with a 600 μm fibre. The laser cladding setup at the University of Nottingham, UK can be seen in Fig. 2. The powder was front fed using argon as the carrier gas, at a flow rate of 10 l min⁻¹. A

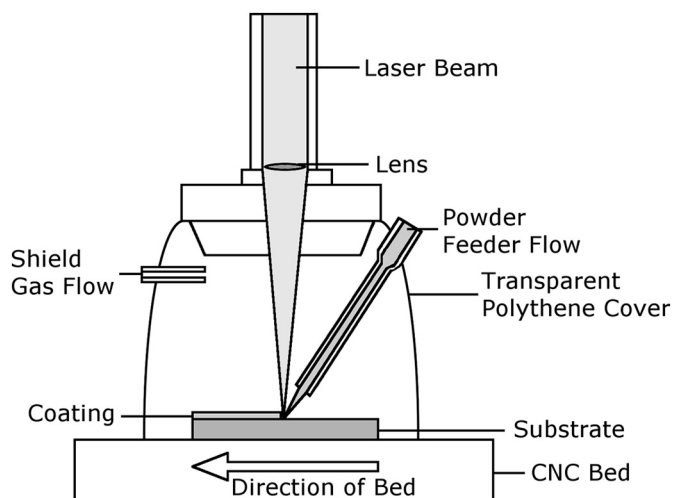


Fig. 2. A schematic of the 2 kW Ytterbium doped fibre laser used at the University of Nottingham in a front fed powder configuration. The laser beam, powder feed setup, substrate positioning and environmental chamber components are all shown.

spot size of 4 mm was achieved using a 20 mm defocus. The powder feed rate, table traverse speed and laser power were varied in different combinations to produce 28 unique coating parameters. These parameters had power ranging from 0.4 to 2 kW; traverse speed varying from 150 to 1200 mm min⁻¹; and powder feed rate varying from 4 to 10 g min⁻¹.

Following the mathematical modelling, one set of optimum processing parameters was selected from this study to develop overlapping tracks. The optimum processing parameters were selected to produce a coating with properties ideal for use in high temperature corrosion applications. The performance of these coatings is studied elsewhere [17]. The same laser set up was used to deposit the NanoSteel SHS 7170 on to a 20 mm × 90 mm × 6 mm 15Mo3 substrate. The coating was produced by laying parallel overlapping beads. An overlap percentage of 60% was used, and successive tracks were all coated in the same direction, maintaining the front fed orientation of the laser.

2.4. Material characterisation

Cross-sections were cut of each of the coating parameter track

perpendicular to the direction of cladding using a SiC precision cutting saw. These sections were mounted in a conductive resin (Bakelite) then ground and polished to a 1 μm diamond finish using standard metallographic preparation techniques. Micrographs were produced using an Eclipse LV100ND optical microscope with NIS elements D software (Nikon Metrology NV, UK). The image analysis software ImageJ (National Institutes of Health, MD) was used to analyse the micrographs to find the cross-sectional area above the substrate, cross-sectional area below the substrate and the porosity fraction. The porosity in the powder was measured using the same preparation techniques and microscope. ImageJ was again used to measure the particle and pore diameter for a sample of 200 particles. The optical techniques used for measuring porosity in the powder were also used to measure porosity in the coatings.

Scanning Electron Microscope (SEM) analysis was carried out on the polished cross sections of the overlapping tracks. An S-3400 N SEM (Hitachi High Technologies, IL, USA) was used in hi-vac mode with a 20 kV beam accelerating voltage. This was accompanied by Energy Dispersive X-ray (EDX) Spectrometry on an x-max 80 mm² spectrometer (Oxford Instruments, UK) to determine the elemental composition within the coating. Micrographs requiring topographical information were taken in Secondary Electron (SE) mode and those requiring elemental distribution were taken using Back Scattered Electron (BSE) mode.

3. Results and discussion

3.1. Powder characteristics

BSE SEM images of the powder cross-section show different contrast regions within the particles. The bulk of the particles contain a dark chromium and boron rich dendrite phase within a lighter matrix. This region is clearly not amorphous. This can be seen in Fig. 3. The amorphous fraction measured in the XRD is likely to arise from the outer shell that has formed on some of the particles. These can be seen in Fig. 3 to be unstructured, and their morphology better seen in Fig. 4. This is contrary to some previous research showing the amorphous fraction arises from the smaller size fraction of the particles [18]. Fig. 3 shows that even the small particles are structured. The dark region in the centre of Fig. 3(a) is a pore formed during powder formation.

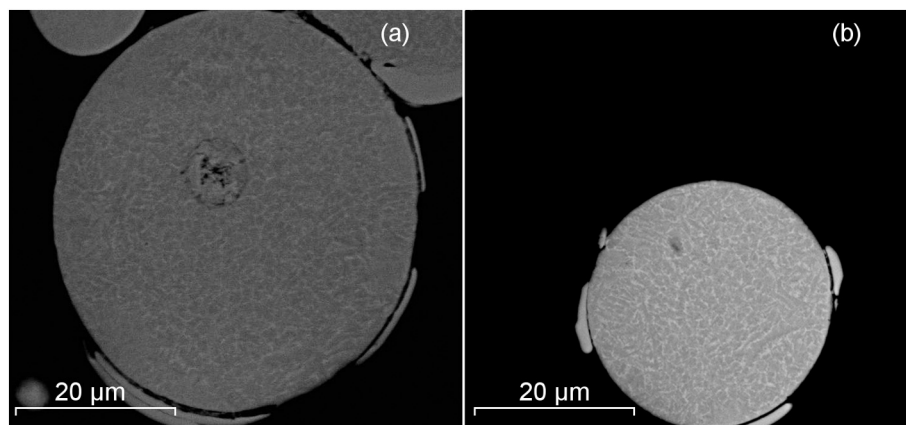


Fig. 3. Cross-sectional BSE micrograph of a large (a) and small (b) powder particle of NanoSteel SHS 7170 showing internal microstructure with bright needle-like structures as well as featureless regions on the exterior of particles.

Parameters.

Symbol	Definition	Symbol	Definition
A_c	Area of clad above substrate	r_s	Laser spot radius
A_m	Area of clad below substrate	s	Distance for pore to travel to surface
A_{max}	Max cross-sectional area of clad	t	Minimum time to escape
A_{obs}	Observed cross-sectional area of clad	$T_{melt(p)}$	Melting temperature of powder
$C_{(p)}$	Specific heat of powder	$T_{melt(s)}$	Melting temperature of substrate
$C_{(s)}$	Specific heat of substrate	T_{room}	Room temperature
D	Area dilution (fraction)	v	Traverse speed of laser
F	Force	v_{pore}	Velocity of rising pore
g	Acceleration due to gravity	V_{pore}	Volume of pore
$L_{f(p)}$	Latent heat of fusion of powder	z	Thickness
$L_{f(s)}$	Latent heat of fusion of substrate	α	Absorbance of powder
n	Number of bins in z	η	Dynamic viscosity of molten powder
$P(r)$	Laser power incident on substrate at melt radius	η_d	Laser power dependent deposition efficiency
P_0	Laser power	η_i	Laser power independent deposition efficiency
PFR	Powder feed rate	η_{melt}	Substrate melting efficiency
r	Melt radius of laser spot	μ	Log-normal distribution mean
r_o	Observed radius of powder particle	$\rho_{(p)}$	Powder density
r_p	True radius of powder particle	$\rho_{(s)}$	Substrate density
r_{pore}	Radius of pore within powder	σ^2	Log-normal distribution variance

3.2. Microstructure of clads

The initial coating characterisation was carried out using optical microscopy of the cross-sections of the clad tracks to examine a larger field of view. There were several key measurements taken to determine suitability of the clads. To achieve a good clad, a produced coating must be thick enough that it can provide sufficient protection. Whilst considering this, a coating must also be as thin as possible whilst maintaining adequate protection to reduce weight and material costs. The measured thickness of the clads ranged from 129 μm to 1554 μm . The area above and below the clad was measured so that area dilution could be calculated from Eq. (1). The definitions of the cross-sectional areas above and below the substrate are defined schematically in Fig. 5. This gave area dilutions ranging from 0% to 48% across the 28 trials performed. For a good clad, dilution must be high enough to allow for good metallurgical bonding of the coating, however low enough that mixing of substrate with coating is not deleterious to performance. Porosity can act as pathways between the external environment and the substrate which the coating is being applied too. As such porosity should be kept to a minimum. The measured porosity in the samples ranged from 1% to 8%.

$$D = \frac{A_m}{A_c + A_m} \quad (1)$$

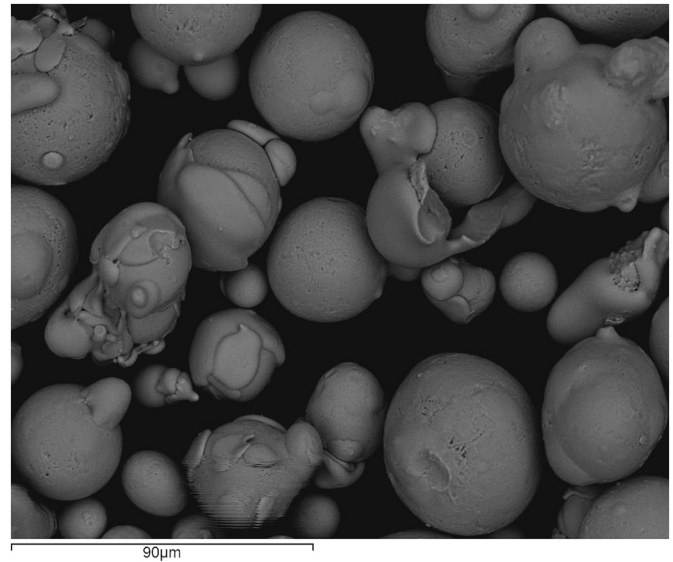


Fig. 4. SE micrograph of the morphology of NanoSteel SHS 7170 powder showing non-spherical morphologies.

BSE micrographs of the clads revealed a similar internal structure across all of the clads. As well as the pores that were clearly visible in the optical micrographs such as in Fig. 5, there is also some phase segregation that can be observed.

3.3. Processing parameter models

3.3.1. Deposition efficiency

By determining a model for the deposition efficiency of the laser cladding process, a calculation can be made to determine the amount of feedstock material lost. Knowing a model means that laser parameters can be modified to minimise this feedstock loss. Laser power independent powder deposition efficiency is the deposition efficiency that is constant across all processing parameters. It can be calculated from the fed mass per unit length and cross-sectional area of the clad measured above the substrate. This deposition efficiency is a ratio of the

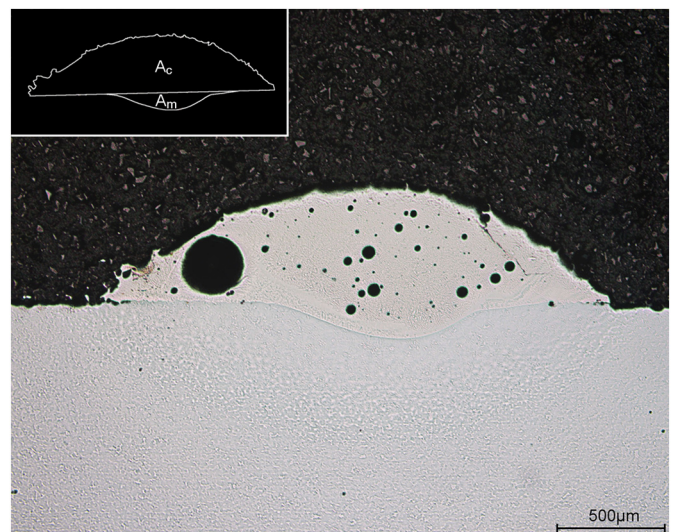


Fig. 5. Optical micrograph of laser clad track clad at a power 800 W, traverse speed 300 mm min^{-1} and powder feed rate of 4 g min^{-1} . The distribution of pores in this sample was typical the 28 trials performed. Top right shows a schematic representation of cross-sectional area above and below substrate.

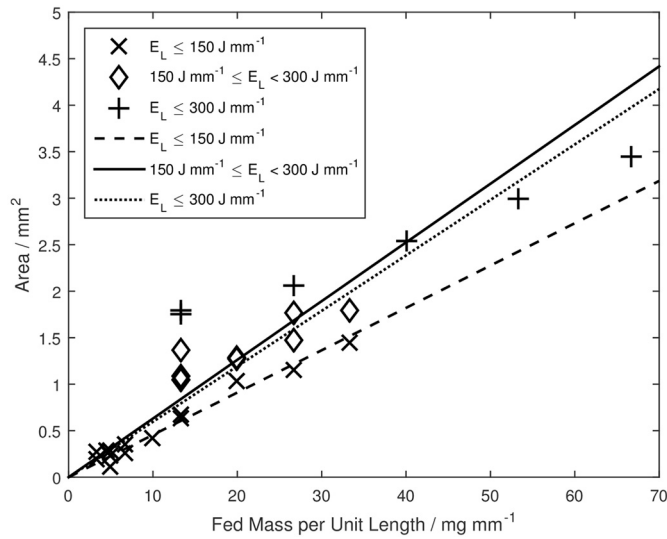


Fig. 6. Observed cross sectional area against fed mass per unit length showing deposition efficiency at different energy per unit lengths (E_L). Data points show experimental data and lines show best fit for calculating deposition efficiency. These lines do not fit the data well. The R^2 value of the set is 0.92.

mass of feedstock provided in a given length and the mass of powder incident on the clad in a given area. This can be seen in Eq. (2).

$$\eta_i = \frac{A_{obs} \nu \rho_{(p)}}{PFR} \quad (2)$$

From a plot of area against fed mass per unit length, as in Eq. (2), the deposition efficiency can be calculated. If it is assumed that deposition efficiency is dependent on the powder feed geometry and properties affecting the powder feed, such as its shape or density, is expected that deposition efficiency will be constant across all coating parameters as these factors remain constant. Conversely, if the powder feed setup were to change, for example through a change in feedstock material, feedstock manufacture or powder feed geometry, this deposition efficiency would need to be recalculated. This recalculated deposition efficiency will encompass the influence that these changed parameters such as feedstock material, feedstock manufacture or powder feed geometry have on the prediction. Taking the density to be 7650 kg m^{-3} [15], Fig. 6 is produced from the 28 trial clad results. It shows the above assumption to be invalid, that deposition efficiency is not solely dependent on fed mass per unit length but that there is also a dependence on energy per unit length. The higher the energy per unit length, the greater the observed area for a given fed mass per unit length. The deposition efficiencies presented at the different energies per unit length are all forced through zero as this is physically significant. If there is zero fed mass per unit length then the observed cross sectional area will be zero.

This difference in observed cross-sectional area at constant fed mass per unit length can be accounted for by assuming a Gaussian beam profile. A Gaussian distribution within the laser spot would produce a region at high radius within the laser beam spot that does not receive enough power to melt incoming powder. Increasing the energy per unit length will increase this melt radius taking it closer to the spot radius and therefore increasing the amount of powder that can be melted. Fig. 7 is a visual representation of this.

Using knowledge of the intensity within a Gaussian power distribution, Eq. (3), it can be shown through simple algebra that the melt radius is given by Eq. (4). Eq. (5) shows the minimum power required to melt the powder. The power dependent deposition efficiency shown in Eq. (6) can therefore be calculated as the ratio of the melt spot area to the laser spot area.

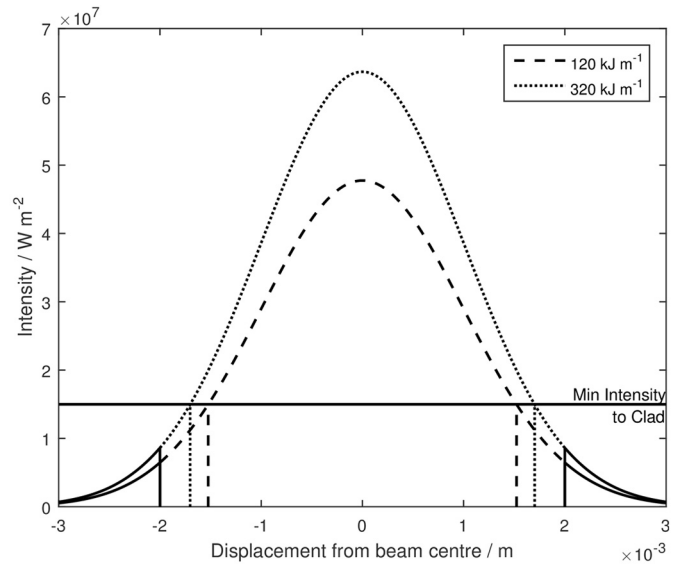


Fig. 7. Beam intensity through beam showing beam spot size with solid lines and melt spot size with broken lines at 120 kJ m^{-1} and 320 kJ m^{-1} . The vertical broken lines show the effective melt radius increasing as the energy per unit length is increased.

$$\frac{P(r)}{P_0} = \exp\left(\frac{-2r^2}{r_s^2}\right) \quad (3)$$

$$r = \frac{r_s}{\sqrt{2}} \sqrt{\ln\left(\frac{P_0}{P(r)}\right)} \quad (4)$$

$$P(r) = PFR(C_{(p)}(T_{melt(p)} - T_{room}) + L_{f(p)}) \quad (5)$$

$$\eta_d = \ln\left(\sqrt{\frac{P_0}{PFR(C_{(p)}(T_{melt(p)} - T_{room}) + L_{f(p)})}}\right) \quad (6)$$

Eq. (6) is true only under two conditions. Firstly, $P_0 \geq P(r)$. Below this limit, the efficiency is zero as no powder can be captured. Secondly, $r \leq r_0$. Beyond this point all powder can be melted and the efficiency is unity. This power dependent deposition efficiency can be used in a correction to Eq. (2). By considering the deposition efficiency to be a

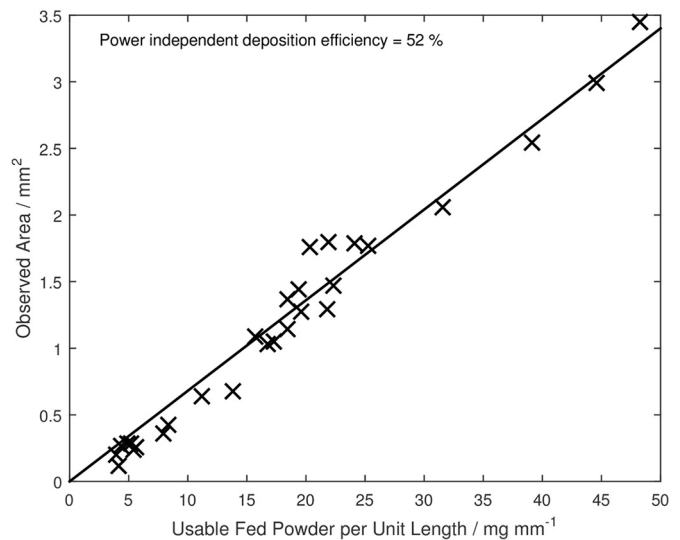


Fig. 8. Determination of power independent deposition efficiency to be 52% from observation of cross-sectional area and determination of usable fed powder per unit length. Prediction has an R^2 value of 0.99.

Table 1
Parameters needed for calculating power dependent deposition efficiency.

Parameter	Value
Melting temperature ($T_{melt(p)}$)	1126 °C [15]
Latent heat of melting ($L_{f(p)}$)	$3 \times 10^5 \text{ J kg}^{-1}$ [15]
Specific heat capacity ($C_{(p)}$)	$750 \text{ J kg}^{-1} \text{ K}^{-1}$ [15]
Room temperature (T_{room})	20 °C

product of the power dependent deposition efficiency and a power independent deposition efficiency, Eq. (2) can be used to produce more accurate predictions. The power independent deposition efficiency accounts for factors such as reflectance of the powder and vaporisation of the melt. In this model it is calculated empirically from the measured data. Calculation of the power independent deposition efficiency can be seen in Fig. 8. The data used to calculate the power dependent deposition efficiency can be found in Table 1.

The thickness of clad required varies depending on application of the final coating. A thicker coating may be required to improve performance, or a thinner coating required for lower cost. However by increasing deposition efficiency, the amount of feedstock required to produce the desired thickness of coating can be decreased. This reduces wastage and therefore total overall material costs. It is discussed above that the power independent deposition efficiency is constant regardless of processing parameters. The power dependent deposition efficiency is maximum when the condition $r \geq r_s$ is met. When this is combined with Eq. (4) and Eq. (5), the criteria for maximum clad efficiency are produced as shown in Eq. (7). Deposition efficiency increases with increasing power and decreasing powder feed rate. When considering parameter selection, it must be noted that as power independent deposition efficiency is not affected by processing parameters, the processing parameters may not be able to be tailored to achieve 100% total deposition efficiency. This is of particular importance in industrial laser cladding systems with very high power (i.e. 20 kW), where power independent deposition efficiency is likely to be maximised at all reasonable operating parameters through Eq. (7). This model is also relevant within these high power industrial laser systems for feedstocks with very high melting temperatures. To achieve the greatest total deposition efficiency, power independent deposition must be maximised, as in Eq. (7).

$$P_0 \geq PFR e^2 (C_{(p)}(T_{melt(p)} - T_{room}) + L_{f(p)}) \quad (7)$$

3.3.2. Dilution

Area dilution can be calculated from knowledge of the cross-sectional area of the clad above and below the surface of the substrate [19]. In welding literature, Eq. (1) is well established for calculating the area dilution. In order to be able to predict the area dilution, it follows from Eq. (1) that we need to be able to predict the cross-sectional area of the clad above and below the surface of the substrate. The cross-sectional area above the substrate is straightforward to calculate from the assumptions used in calculating the deposition efficiency above. This can be seen in Eq. (8), a rearrangement of Eq. (2). The cross-sectional area of the clad below the substrate can be calculated simply from the energy per unit length incident on the substrate and the volume of substrate material that energy per unit length is sufficient to melt. This is shown in Eq. (9) from the heat capacity equation. The final addition to this prediction is that the energy per unit length reaching the substrate is the total energy per unit length provided by the laser minus the energy required to melt the clad material. This gives a more comprehensive prediction of the cross-sectional area below the substrate surface seen in Eq. (10).

$$A_c = \frac{PFR}{v\rho_{(p)}} \eta_d \eta_i \quad (8)$$

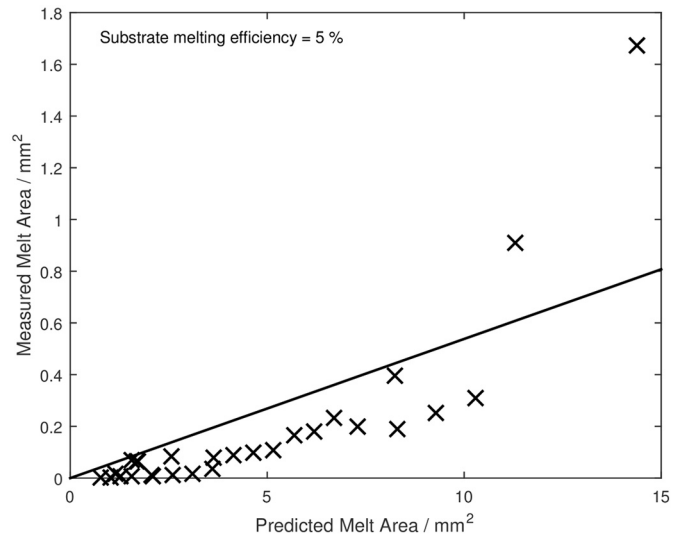


Fig. 9. Determination of substrate melting efficiency from plot of empirically observed melt area against prediction of melt area. The solid line shows the ideal relationship where the predicted values agree with those measured. The substrate melting efficiency is calculated from the gradient of this line.

$$A_m = \left(\frac{P}{v} \right)_{\text{Substrate}} \frac{1}{\rho_{(s)}(C_{(s)}\Delta T_{(s)} + L_{f(s)})} \quad (9)$$

$$A_m = \frac{\frac{P_0}{v} - \frac{PFR(C_{(p)}\Delta T_{(p)} + L_{f(p)})}{v}}{\rho_{(s)}(C_{(s)}\Delta T_{(s)} + L_{f(s)})} \quad (10)$$

There are three factors to be considered when working out the proportion of the system energy that goes into melting the substrate. The first of these factors is absorbance of the powder. This is the fraction of the incoming energy that the powder particle is able to absorb, with any remaining fraction being reflected away and lost. This loss factor reduces the total power going into the clad-substrate system. It is assumed that all power is incident on the powder, and excess heating is transferred to the substrate by conduction. A value for absorbance of 0.12 was used [20]. The second loss factor comes from the deposition efficiency that was calculated above. This loss factor can be affected by powder feed geometry as well as a number of other variables, which have been previously outlined in Section 3.3.1 where deposition efficiency is discussed. The final factor is substrate melting efficiency. This encompasses all of the remaining loss factors such as heat flow within the substrate, geometric effects and conductive heat losses in the system, all factors that will vary greatly between laser setups. This is calculated empirically by comparing the predicted cross sectional area by the measured cross-sectional area. It is expected that this factor will encompass such losses as heating of the substrate to areas that do not melt and radiation of energy away from the clad. Combining these three factors, the predicted area of the clad below the substrate can be calculated using Eq. (11). This was used to produce Fig. 9 using the data in Table 1 and Table 2. A value for latent heat of melting for 15Mo3 could not be found in the literature so a value for low alloy steel was used as a substitute. Fig. 9 plots the experimentally observed cross-sectional area of the clads against their predicted values as calculated from Eq. (11).

Table 2
Parameters needed for calculating substrate melting efficiency.

Parameter	Value
Melting temperature ($T_{melt(s)}$)	1370 °C [21]
Latent heat of melting ($L_{f(s)}$)	$3 \times 10^5 \text{ J kg}^{-1}$
Specific heat capacity ($C_{(s)}$)	$500 \text{ J kg}^{-1} \text{ K}^{-1}$ [21]
Density ($\rho_{(s)}$)	8000 kg m^{-3} [21]

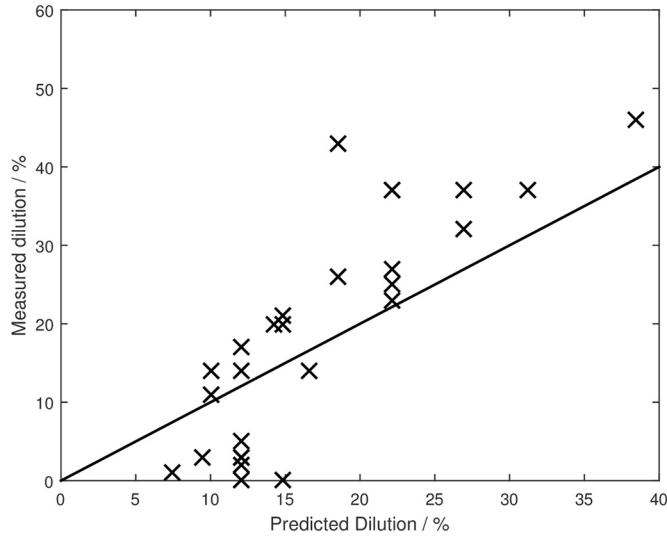


Fig. 10. Comparison of empirically measured dilution in samples compared to the dilution predicted at corresponding processing parameters with the line showing a perfect agreement.

The line shows the point at which the two values match. This was used to determine the substrate melting efficiency as 5%.

$$A_m = \frac{\eta_{melt} \left(\alpha \frac{P_0}{v} - \frac{\eta_i PFR(C_{(p)} \Delta T_{(p)} + L_{f(p)})}{v} \right)}{\rho_{(s)} (C_{(s)} \Delta T_{(s)} + L_{f(s)})} \quad (11)$$

By combining Eq. (1), Eq. (8) and Eq. (11), a predictive equation for the dilution can be found as Eq. (12). This has been used to compare the predicted dilution to the measured area dilution as can be seen in Fig. 10. It can be seen from this that as power increases, so does dilution, and that the inverse is true of powder feed rate. This allows dilution to be fine-tuned using only two parameters. If strong adhesion is needed, power can be increased and powder feed rate decreased, however if low dilution is required, power can be minimised.

$$D = \frac{\eta_{melt} \alpha P_0 - \eta_{melt} \eta_i PFR(C_{(p)} \Delta T_{(p)} + L_{f(p)})}{\eta_{melt} \alpha P_0 + PFR \left(\frac{\rho_{(s)}}{\rho_{(c)}} (C_{(s)} \Delta T_{(s)} + L_{f(s)}) \eta_d \eta_i - \eta_{melt} \eta_i (C_{(p)} \Delta T_{(p)} + L_{f(p)}) \right)} \quad (12)$$

3.3.3. Porosity

When coating materials, especially with powders, porosity can arise in the coating. Depending of the final application of the coating, porosity may be desirable, or undesirable. In either case it being able to predict the source and amount of porosity is important. Empirical models exist for predicting porosity, however they are material dependent and do not identify the causes of porosity. By developing a model to calculate the source of porosity from a single cause, a more accurate prediction of porosity can be made. There are two possible sources for porosity that can be considered. The first is a geometric effect arising when the powder particles do not fully melt, and create voids when placed in the laser spot. When looking at the cross-sectional images of the coatings used, such as Fig. 5, there are no signs that the powder particles have not been fully melted and there is no evidence of their original shape in the clad. The voids all have a very symmetrical shape all suggesting that the pores are not caused by unmelted particles. The other option is that the pores are formed by outgassing. This is related to gas being released from the powder when it is melted. This released gas is trapped in bubbles as the melt solidifies.

It has been shown above, as the fed mass per unit length increases, so does the observed cross-sectional area. This would result in the porosity percentage due the mechanism above being constant across all

fed mass per unit lengths. The method by which pores may escape could be by rising to the surface of the melt before it solidifies. This would be dependent of two factors; the speed at which the melt solidifies and the speed at which the pores rise. The speed at which the melt solidifies is dependent on the rate of heat loss from the melt. Assuming this is constant then the parameter that will affect this is the energy per unit mass. So long as enough energy is supplied to melt the incoming powder, any excess energy is assumed to heat the melt (with an appropriate loss factor). The greater this overheating, the longer the melt will take to cool below its melting point and solidify, suggesting the porosity percentage will be linearly dependent on energy per unit length. The speed at which the pores rise is dependent on two factors; the buoyancy of the pores and the drag acting on the pores.

The buoyancy of the pores can be calculated using Eq. (13). When this is combined with stokes law shown in Eq. (14), the terminal velocity of the particle can be calculated by Eq. (15). By assuming that acceleration of the bubbles is instantaneous from the point at which they form to their terminal velocity, a minimum time to escape can be calculated by Eq. (16).

$$F = \frac{4}{3} \rho_{(p)} \pi r_{pore}^3 g \quad (13)$$

$$F = 6\pi\eta r_{pore} v_{pore} \quad (14)$$

$$v_{pore} = \frac{2\rho_{(p)} r_{pore}^2 g}{9\eta} \quad (15)$$

$$t = \frac{9\eta s}{2\rho_{(p)} r_{pore}^2 g} \quad (16)$$

Using the values in Table 3, a minimum timescale to escape can be calculated at ~ 0.06 s. This is shorter than the typical solidification time at these temperatures calculated in the literature for laser cladding at 0.1 s [22]. The calculated minimum timescale to escape is shorter than the typical solidification time to escape, initially suggesting that no porosity should be observed. However it must be taken into account that this is a minimum time to escape and the true value will be higher than this. It must also be taken into account that the calculation of this value has many limitations. The value for viscosity was not measured directly, nor could a true value be found in the literature. Instead, the viscosity of $Fe_{0.8}Cr_{0.2}$ at 1600 °C, $\sim 150\%$ of the melting temperature, was used. Whilst this is not ideal, it is known that highly alloyed materials tend to have higher viscosities than their lower alloyed counterparts. As such, the use of $Fe_{0.8}Cr_{0.2}$ in this calculation will likely lower the viscosity producing a shorter minimum time to escape than the true value, further supporting the outgassing theory. Furthermore, density of melt is taken to be the same as that which is measured at room temperature. The true value for density is likely lower than this, following the trend of other materials in reducing density as temperature increases. A reduced density would result in a longer minimum time to escape, again supporting the outgassing theory. The powder is produced to a maximum particle radius of 27 μm . The larger a pore, the greater the time to escape will be, as can be seen in Eq. (16). As such a maximum pore size was used equal to the maximum radius of the powder particles. A minimum distance was also used from the minimum clad height produced.

Table 3

Parameters needed for calculating minimum timescale to escape.

Parameter	Value
Dynamic viscosity (η)	5.5×10^{-3} Pa s [23]
Distance (s)	0.129 mm
Density ($\rho_{(p)}$)	7590 kg m $^{-3}$ [24]
Room temperature (T_{room})	20 °C
Gravitational acceleration (g)	9.81 m s $^{-2}$
Radius of bubble (r_{pore})	27 μm

In order to further validate the outgassing theory, a comparison must be made between the porosity present in the feedstock powder and the porosity found in the coating. If these values are the same, then it supports the theory that porosity is caused by outgassing. In order to do this, an accurate volume of pores within the feedstock must be estimated. When looking at a 2D section through a particle, the depth at which the section is taken is unknown, and therefore the observed radius of the particle may not necessarily be representative of the true radius of the particle. We must first start with the assumption that sample preparation is perfect, and as such, the thickness at which a section is taken, z , has equal probability of occurring at all thicknesses. This is described by the cumulative distribution function shown in Eq. (17). This thickness can be used to relate the constant true radius, r_{pore} , to the random variable, the observed radius in the given section, r_o , by Eq. (18).

$$F_z(z) = P(Z \leq z) = \begin{cases} 0 & z \leq 0 \\ \frac{z}{r_{pore}} & 0 < z < r_{pore} \\ 1 & z \geq r_{pore} \end{cases} \quad (17)$$

$$r_o = \sqrt{r_{pore}^2 - Z^2} \quad (18)$$

In order to predict a distribution of observed radiuses in a range of particles, it is important to first be able to predict the distribution of observed radiuses in a sample of identical particles with the same radiuses. To do this we need to produce the cumulative distribution function shown in Eq. (19). Taking Eq. (19), and substituting Eq. (17) and Eq. (18), we can produce the cumulative distribution function shown in Eq. (20). By differentiating this cumulative distribution, the probability density function of observed radius can be found for a set of random sections taken from a sample of identical particles. This Probability Density Function (PDF) is shown in Eq. (21), and can be seen graphically in Fig. 11.

$$F_{r_o}(r) = P(r_o \leq r) \quad (19)$$

$$F_{r_o}(r) = 1 - \frac{\sqrt{r_{pore}^2 - r^2}}{r_{pore}} \text{ for } 0 \leq r \leq r_{pore} \quad (20)$$

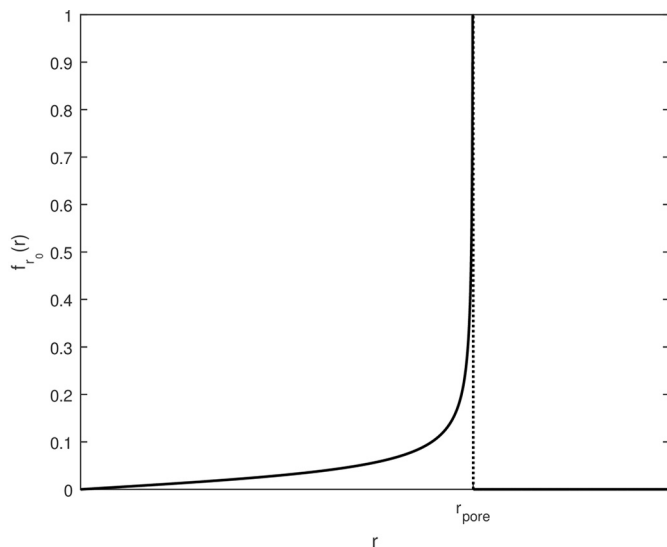


Fig. 11. The Probability Density Function characterises the distribution of the observed radius from taking random cross sections through pores with true radius r_{pore} .

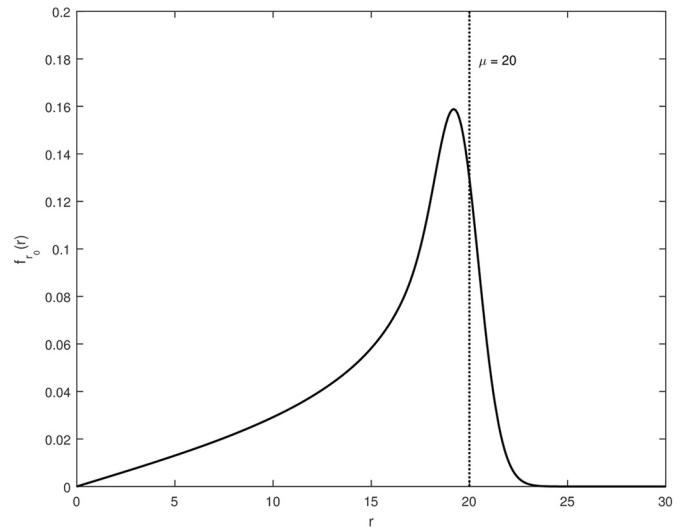


Fig. 12. Probability density function for the observed pore radius, from taking random cross sections through randomly sampled pores whose true radii follow a log-normal distribution with mean $\mu = 20 \mu\text{m}$ and variance $\sigma^2 = 1$. The expression for this pdf is shown in Eq. (23).

$$F_{r_o}f_{r_o}(r) = \begin{cases} 0 & r < 0 \\ \frac{r}{r_{pore}} \left(\frac{1}{\sqrt{r_{pore}^2 - r^2}} \right) & 0 \leq r \leq r_{pore} \\ 0 & r > r_{pore} \end{cases} \quad (21)$$

The special case of a sample distribution containing only particles of a single true radius, is solved in Eq. (21). Empirical data shows that many gas atomised powders fit a log-normal distribution, and the assumption is made that the distribution of pores within the powder is also log-normal [25]. In order to determine the observed radius distribution in a log-normally distributed sample of particles, the probability density function of which is described by Eq. (22), the true probability density function must be convolved with that of a sample with uniform true radius. This is described in Eq. (23), and is visually represented in Fig. 12.

$$f_{r_{pore}}(r) = \frac{1}{r \sqrt{2\pi \ln\left(1 + \frac{\sigma^2}{\mu^2}\right)}} \exp\left(-\frac{\left(\ln \frac{r \sqrt{1 + \frac{\sigma^2}{\mu^2}}}{\mu}\right)^2}{2 \ln\left(1 + \frac{\sigma^2}{\mu^2}\right)}\right) \quad (22)$$

$$f_{r_o}(r) = \int_0^\infty \frac{1}{r_{pore} \sqrt{2\pi \ln\left(1 + \frac{\sigma^2}{\mu^2}\right)} (r_{pore}^2 - r^2)} \exp\left(-\frac{\left(\ln \frac{r \sqrt{1 + \frac{\sigma^2}{\mu^2}}}{\mu}\right)^2}{2 \ln\left(1 + \frac{\sigma^2}{\mu^2}\right)}\right) dr \quad (23)$$

Eq. (23) describes how the probability density function of the observed particle radius depends on the mean, μ , and variance, σ^2 , of an underlying log-normal distribution of particle radius. Calculating the porosity fraction requires μ , which in practice is not directly observed, however it can be inferred by fitting the distribution in Eq. (23) to the empirical distribution of observed particle radius. We fit this distribution by minimising, with respect to μ and σ^2 , the Kolmogorov-Smirnoff distance, shown in Eq. (24), between F_{r_o} , which is the CDF corresponding to the PDF in Eq. (23), and $F(r)$, which is the empirical CDF of the observed particle radius.

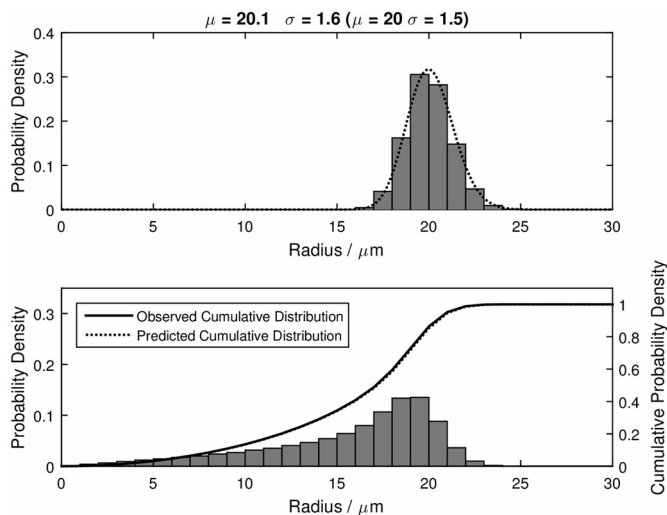


Fig. 13. Probability Density of true pore distribution (top) and observed pore radius (bottom) within a simulated data set along with the predicted probability distribution (top) and predicted cumulative probability distribution in solid line and true cumulative probability distribution in dotted line (bottom) on a 101×101 grid with 10,000 samples.

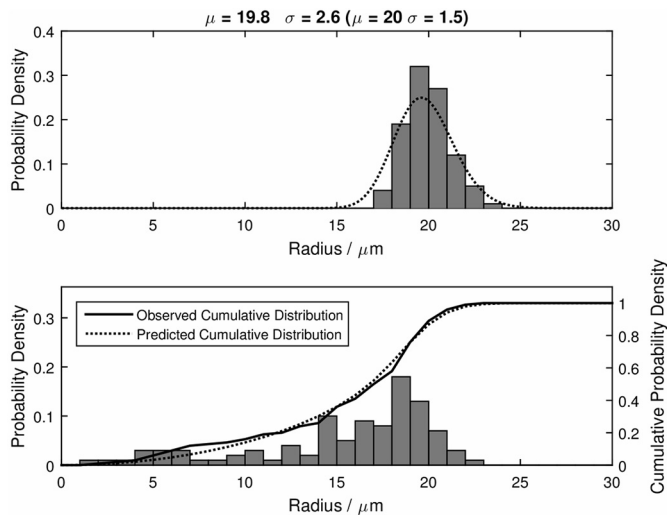


Fig. 14. Probability Density of true pore distribution (top) and observed pore radius (bottom) within a simulated data set along with the predicted probability distribution (top) and predicted cumulative probability distribution in solid line and true cumulative probability distribution in dotted line (bottom) on a 101×101 grid with 100 samples.

$$|F_0(\mathbf{r}; \mu, \sigma) - F(\mathbf{r})| \tag{24}$$

This can be achieved by computing Eq. (24) for a grid of (μ, σ^2) values and identifying for which it is smallest. A final matrix size of 101×101 was chosen with the values of mean and variance equally spaced between the limits. The resultant fit is shown in Fig. 13. It can be seen that the predicted value is incorrect by 0.5% for the mean and 8% for the variance. As the mean is the value that we are looking for it was decided that the model with this grid size was a good fit. To check the validity of the model further, the number of particles needed to allow for an accurate prediction was calculated. This was done by running simulated data sets of varying sizes and comparing the predicted input to the true input. Sample sizes were tested at increasing orders of magnitude. Whilst samples sizes of the order 10^1 varies greatly from the true mean, at samples sizes of the order 10^2 and above the difference between the true input and the predicted input varied by $\sim 0.2 \mu\text{m}$. as such a sample size of ~ 100 particles was deemed suitable to produce

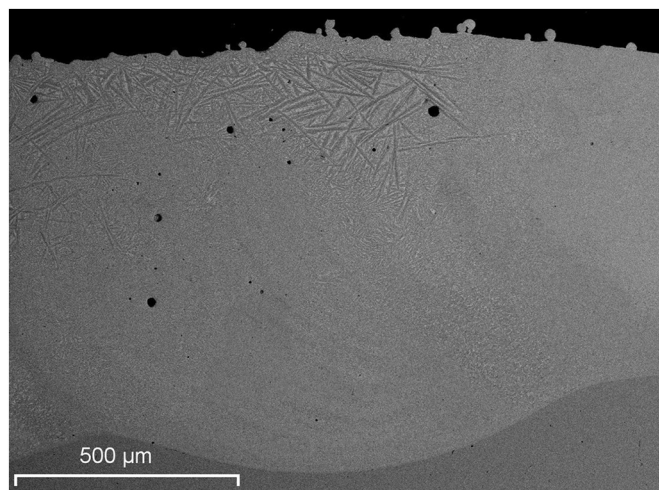


Fig. 15. Back Scattered Electron section of overlapping clad at laser pass boundary for overlap coating deposited at 1000 W power, 300 mm min^{-1} traverse speed and 4 g min^{-1} powder feed rate. The dilution and porosity of 7% and 0.7% respectively can be visualised.

reliable results. The fit of a 100 particle simulation can be seen in Fig. 14.

Having shown that the method works well using simulated data, it was carried out on a sample of 80 pores. Using the process outlined, a mean pore diameter for the sample was calculated to be $6.2 \mu\text{m}$. Using this value, combined with the mean particle diameter of the original powder sample, the porosity volume fraction has been calculated at 8.5%. Measurements of the porosity in the produced clad produced an average of $3.4\% \pm 0.4\%$, just below the value calculated. This discrepancy may be accounted for by the escape time calculated earlier in this section. As the escape time for trapped pores, and the solidification time the clad are similar time scales, it is reasonable to expect some of these pores to have escaped. From this, it is concluded that the porosity is caused by outgassing and as such processing parameter optimisation will not affect the final porosity of the clad.

3.4. Microstructure of overlap clad

Based on the parameters determined above, the parameters were selected to produce the most desirable clad. The porosity of the clad is not determined by the processing parameters and as such no optimisation of porosity is possible for the given feedstock. To minimise dilution, the power must be as low as possible and the powder feed rate as high as possible, however to maximise the deposition efficiency, Eq. (7) must be satisfied requiring power to be as high as possible and powder feed rate as low as possible. Two overlapping clad sections were produced, the first with a power of 800 W, traverse speed of 300 mm min^{-1} , and powder feed rate of 4 g min^{-1} . The second had a power of 1000 W, traverse speed of 300 mm min^{-1} , and powder feed rate of 4 g min^{-1} . A section of the first clad produced can be seen in Fig. 15. Of the two clads produced, the most successful was the clad produced using a power of 1000 W. The power independent capture efficiency calculated from this overlap trial alone is 43%, slightly below the value predicted by the model of 52%. The dilution in this clad is measured to be 7%, compared to the model prediction of 13%. The porosity in the overlap clad was lower than expected at 0.7%.

4. Conclusion

In this study, the Fe-Cr-B alloy NanoSteel SHS 1770 was deposited onto a low alloy steel substrate via laser cladding. The aim was to develop the optimal overlapping coating and produce a predictive

mathematical model for determining the processing parameters needed to produce this. The following conclusions can be made:

- Powder deposition efficiency comprises two parts. The first is parameter independent and is calculated empirically. The second is dependent on the ratio of laser power to powder feed rate. Maximum deposition efficiency occurs when the inequality $P_0 \geq PFR e^2 (C_{(p)}(T_{melt(p)} - T_{room}) + L_{f(p)})$ is satisfied.
- Dilution can be predicted with Eq. (12). It is dependent on laser power and powder feed rate, as well as material dependent factors such as melting point and specific heat capacity. Dilution is minimised when laser power is minimised and powder feed rate is maximised. A substrate melting efficiency must be calculated empirically to predict dilution.
- The porosity is shown to be caused by outgassing, and therefore is independent of processing parameters. A method for calculating expected porosity within powders has been produced given a cross-section of powder particles.
- The models have been validated through the production of overlapping clads and comparison of their measured parameters to those predicted by the model.

5. Acknowledgments

This work was supported by the Engineering and Physical Sciences Research Council [grant number EP/L016362/1]; in the form of an EngD studentship and industrial funding from Uniper Technologies Limited.

References

- [1] A.J. Pinkerton, L. Li, The significance of deposition point standoff variations in multiple-layer coaxial laser cladding (coaxial cladding standoff effects), *Int J Mach Tool Manu* 44 (2004) 573–584.
- [2] H. Tan, W. Shang, F. Zhang, A.T. Clare, X. Lin, J. Chen, Process mechanisms based on powder flow spatial distribution in direct metal deposition, *J. Mater. Process. Technol.* 254 (2018) 361–372.
- [3] M. Ansari, R.S. Razavi, M. Barekat, An empirical-statistical model for coaxial laser cladding of NiCrAlY powder on Inconel 738 superalloy, *Opt. Laser Technol.* 86 (2016) 136–144.
- [4] U. de Oliveira, V. Ocelik, J.T.M. De Hosson, Analysis of coaxial laser cladding processing conditions, *Surf. Coat. Technol.* 197 (2005) 127–136.
- [5] M. Berekat, R. Shoja Razavi, A. Ghasemi, Nd:YAG laser cladding of Co–Cr–Mo alloy on γ -TiAl substrate, *Opt. Laser Technol.* 80 (2016) 145–152.
- [6] V. Ocelik, U. De Oliveira, M. de Boer, J.T.M. De Hosson, Thick Co-based coating on cast iron by side laser cladding: Analysis of processing conditions and coating properties, *Surf. Coat. Technol.* 201 (2007) 5875–5883.
- [7] Y.W. Sun, M.Z. Hao, Statistical analysis and optimization of process parameters in Ti6Al4V laser cladding using Nd:YAG laser, *Opt. Lasers Eng.* 50 (2012) 985–995.
- [8] N. Ahmed, K.T. Voisey, D.G. McCartney, Investigation into the effect of beamshape on melt pool characteristics using analytical modelling, *Opt. Lasers Eng.* 48 (2010) 548–554.
- [9] M. Picasso, C.F. Marsden, J.D. Wagniere, A. Frenk, M. Rappaz, A simple but realistic model for laser cladding, *Metall. Mater. Trans. B Process Metall. Mater. Process. Sci.* 25 (1994) 281–291.
- [10] I. Tabernero, A. Lamikiz, S. Martinez, E. Ukar, L.N.L. de Lacalle, Modelling of energy attenuation due to powder flow-laser beam interaction during laser cladding process, *J. Mater. Process. Technol.* 212 (2012) 516–522.
- [11] H.R. Shercliff, M.F. Ashby, The prediction of case depth in laser transformation hardening, *Metall. Trans. A.* 22 (1991) 2459–2466.
- [12] P.H. Steen, P. Ehrhard, A. Schussler, Depth of melt-pool and heat-affected zone in laser-surface treatments, *Metall. Mater. Trans. A* 25 (1994) 427–435.
- [13] H.J.G. Gundersen, E.B. Jensen, Particle sizes and their distributions estimated from line- and point-sampled intercepts. Including graphical unfolding, *Journal of Microscopy* 131 (1983) 291–310.
- [14] H.J.G. Gundersen, E.B. Jensen, Steriological estimation of the volume weighted mean volume of arbitrary particles observed on random sections, *J. Microsc.* 138 (1985) 127–142.
- [15] K. Chokethawai, Microstructural Evolution in Fe-Cr-B based Alloy Powder and Thermally Sprayed Coatings and Their Wear Performance, (2010).
- [16] Sandvik Materials Technology, Sandvik 15Mo3 tube and pipe, Seamless Datasheet, 2017.
- [17] L. Reddy, P. Shipway, C. Davis, T. Hussain, HVOF and laser-cladded Fe-Cr-B coating in simulated biomass combustion: microstructure and fireside corrosion, *Oxid. Met.* 87 (2017) 825–835.
- [18] K. Chokethawai, D.G. McCartney, P.H. Shipway, Microstructure evolution and thermal stability of an Fe-based amorphous alloy powder and thermally sprayed coatings, *J. Alloys Compd.* 480 (2009) 351–359.
- [19] B. Song, T. Hussain, K.T. Voisey, Laser cladding of Ni50Cr: a parametric and dilution study, *Phys. Procedia* 83 (2016) 706–715.
- [20] T.J. Wieting, J.L. DeRosa, Effects of surface condition on the infrared absorptivity of 304 stainless steel, *J. Appl. Phys.* 50 (1979) 1071–1078.
- [21] SteelSS, Data Table for: High alloy: 16Mo3, (2011).
- [22] V. Ocelik, I. Furar, J.T.M. De Hosson, Microstructure and properties of laser clad coatings studied by orientation imaging microscopy, *Acta Mater.* 58 (2010) 6763–6772.
- [23] R. Novakovic, J. Brillo, Thermodynamics, thermophysical and structural properties of liquid Fe-Cr alloys, *J. Mol. Liq.* 200 (2014) 153–159.
- [24] I. ShipMate, Material Safety Data Sheet: SHS 7170 Thermal Spray Powder, The NanoSteel Company Inc., Providence, Rhode Island, 2011.
- [25] O.D. Neikov, S.S. Naboychenko, I.V. Murashova, V.G. Gopienko, I.V. Frishberg, D.V. Lotoko, Handbook of Non-ferrous Metal Powders, 1st ed., Elsevier, UK, 2009.